Elastic Properties of Flux-Line Arrays in High Transition Temperature Superconductors Probed by Two-Sided Decoration

Seokwon Yoon, Zhen Yao, Hongjie Dai, Charles M. Lieber

Science, New Series, Volume 270, Issue 5234 (Oct. 13, 1995), 270-273.

Stable URL:
http://links.jstor.org/sici?sici=0036-8075%2819951013%293%3A270%3C270%3AEPOFAI%3E2.0.CO%3B2-V

Elastic Properties of Flux-Line Arrays in High Transition Temperature Superconductors Probed by Two-Sided Decoration

Seokwon Yoon,* Zhen Yao, Hongjie Dai, Charles M. Lieber†

The elastic constants of magnetic flux-line lattices in copper oxide superconductors have remained uncharacterized despite their essential role in determining important phenomena such as melting. Here the absolute values of the elastic moduli of flux-line arrays have been probed by correlating the positions of individual flux lines emerging from opposite sides of $Bi_2Sr_2CaCu_2O_8$ (BSCCO) superconductors. These experiments demonstrate that the compressional and shear moduli of the flux-line lattice are three orders of magnitude smaller than the values predicted by standard models. The origin of these changes in the moduli and the general applicability of this approach to other materials are discussed. In addition, there is a remarkable correspondence between the excitations of the flux-line arrays and those of superfluid helium.

Exploiting the high-temperature superconductivity exhibited by copper oxide materials remains a great challenge to fundamental and applied research (*1*, *2*). This challenge arises in large part from the propensity of magnetic flux lines in these type-II superconductors to flow and dissipate energy in the presence of currents (*1*–*6*). To control rationally such deleterious behavior ultimately requires a fundamental understanding of the structural properties of flux-line arrays. In particular, knowledge of the elastic moduli could provide important insight into this problem because they are central to calculations of thermal fluctuations, melting, and the effects of weak pinning (*2*, *3*). Indeed, many theoretical studies of the flux-line lattice elastic moduli have been reported (*2*–*6*); however, no direct experimental evaluations are available to test these predictions.

Herein we report studies of the elastic properties of flux-line arrays in BSCCO superconductors done with a recently developed technique (*7*) that enables the positions of individual flux lines on both sides of a sample to be visualized and correlated. This approach is motivated by the understanding that the propagation of thermally excited fluctuations in the flux lines as they cross a sample will depend on the elastic properties of the array of flux lines (*6*, *8*). By analyzing the density and orientational correlations of the flux lines as they pass through samples, we have been able to extract the absolute values of the compressional (c_{11}), tilt (c_{44}), and shear (c_{66}) moduli for flux-line arrays in BSCCO as a function of the magnetic field B. These data exhibit large deviations from general theoretical predictions for anisotropic superconductors, and thus should be considered in the analyses of melting and pinning of the flux-line lattice in the copper oxide materials.

The Bitter technique has been used previously to decorate individual magnetic flux lines emerging from one surface of a superconductor (*9*–*11*). We have recently extended this technique to provide three-dimensional (3D) information simply by decorating simultaneously the two opposite sides of a sample; that is, double-sided decoration (*7*). Typical images of the same xy location from two sides of BSCCO samples decorated in fields of 5, 12, and 24 G are shown in Fig. 1. In these images, each flux-line position corresponds to the vertex formed by bonds drawn from the flux line to its nearest neighbors. These images show that at 12 and 24 G, the flux-line arrays are relatively well ordered and display a good correspondence of topological defects through the samples, in agreement with earlier work (*7*). At 5 G, where the flux-line array is in a highly disordered liquid-like state, there is still a good correspondence of topological defects and individual flux lines across the sample. There are, however, differences at the lattice constant scale in positions of individual flux lines and defect topologies crossing the sample, which indicate that the flux lines

Division of Applied Sciences and Department of Chemistry, Harvard University, Cambridge, MA 02138, USA.

*Present address: Department of Physics, Catholic University, Bucheon, Korea 422-743.
†To whom correspondence should be addressed.

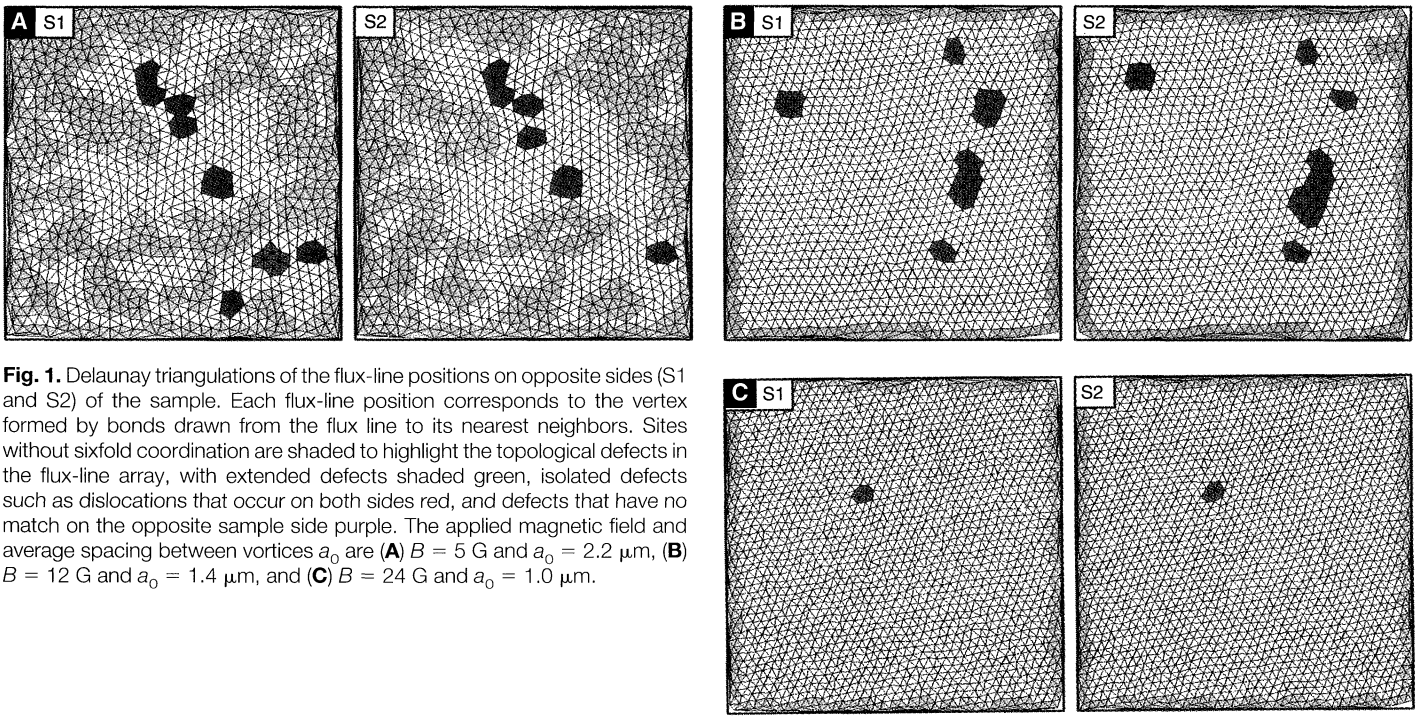

Fig. 1. Delaunay triangulations of the flux-line positions on opposite sides (S1 and S2) of the sample. Each flux-line position corresponds to the vertex formed by bonds drawn from the flux line to its nearest neighbors. Sites without sixfold coordination are shaded to highlight the topological defects in the flux-line array, with extended defects shaded green, isolated defects such as dislocations that occur on both sides red, and defects that have no match on the opposite sample side purple. The applied magnetic field and average spacing between vortices a_0 are (**A**) B = 5 G and a_0 = 2.2 μm, (**B**) B = 12 G and a_0 = 1.4 μm, and (**C**) B = 24 G and a_0 = 1.0 μm.

meander as they traverse these samples.

The central result of this paper is the quantitative evaluation of the absolute values of the elastic moduli versus magnetic field obtained from an analysis of flux-line meandering across samples. The relation between thermally excited flux-line meandering and the elastic moduli has been derived previously with a hydrodynamic model (*12, 13*). For a sample of finite thickness L, the 3D density correlation function relevant to our two-sided decoration data is

$$S(q_\perp, L) = S_2(q_\perp)R(q_\perp, L) \qquad (1)$$

where $S_2(q_\perp)$ is the density correlation function calculated from one surface, $R(q_\perp, L) = [\cosh(L/\xi(q_\perp))]^{-1}$ measures the loss of translational order across the sample, and $q_\perp$ is the in-plane wave vector. The correlation length $\xi_\parallel(q_\perp)$ can be expressed in terms of the ratio of the compressional $[c_{11}(q_\perp)]$ and the tilt $[c_{44}(q_\perp)]$ moduli of the flux-line array

$$\xi_\parallel(q_\perp) = \sqrt{\frac{c_{44}(q_\perp)}{c_{11}(q_\perp)}}\,\frac{1}{q_\perp} \qquad (2)$$

and $S_2(q_\perp)$ can be expressed in terms of the product of the compressional and tilt moduli

$$S_2(q_\perp) = \frac{n_0 k_B T}{2\sqrt{c_{11}(q_\perp)c_{44}(q_\perp)}}\,q_\perp \qquad (3)$$

where n_0 is the average density of flux lines, k_B is the Boltzmann constant, and T is temperature (*14*). This analysis predicts that $1/\xi_\parallel(q_\perp)$ and $S_2(q_\perp)$ should go linearly to zero as $q_\perp$ goes to zero, and shows that the ratio and product of $c_{11}(q_\perp \rightarrow 0) \equiv c_{11}$ and $c_{44}(q_\perp \rightarrow 0) \equiv c_{44}$ can be obtained from the slopes of these lines.

Because $S(q_\perp, L)$ and $S_2(q_\perp)$ can be calculated directly from our two-sided decoration data, it is possible to determine c_{11} and c_{44}. Plots of $\cosh^{-1}[S_2(q_\perp)/S(q_\perp, L)]$ and $S_2(q_\perp)$ calculated from the two-sided decoration data in the disordered state at 5 G and in the more ordered state at 12 G are shown in Fig. 2. The long-wavelength (small $q_\perp$) behavior of these data exhibit the linear dependence on $q_\perp$ expected from the hydrodynamic model. The linear regions of $\cosh^{-1}[S_2(q_\perp)/S(q_\perp, L)]$ and $S_2(q_\perp)$ yield $L\sqrt{c_{11}/c_{44}}$ and $n_0k_BT/2\sqrt{c_{11}c_{44}}$ from which we obtain the absolute values of the moduli: at 5 G, $c_{11} = 1.8 \times 10^{-3}$ and $c_{44} = 1.0$ G^2, and at 12 G, $c_{11} = 8.0 \times 10^{-3}$ and $c_{44} = 4.8$ G^2 (*15*).

A similar approach can be used to measure the shear modulus c_{66} as a function of magnetic field, by determining the propagation of orientational order through the samples (*12*). Physically, the degree to which the orientation of the Bitter patterns from the two sample sides line up is indicative of how well the flux array resists shear deformations. The bond orientational correlation function $G_6(q_\perp, L)$ correlating the flux-line images from both sample sides is given by $G_6(q_\perp, L) = G_6(q_\perp)R_H(q_\perp, L)$, where $G_6(q_\perp, L)$ is the orientational correlation function calculated from a single side and $R_H(q_\perp, L) = [\cosh(L/\xi_H(q_\perp))]^{-1}$ describes the decay of flux-line orientational correlation through the sample with correlation length $\xi_H(q_\perp)$ (*16*)

$$\xi_H(q_\perp) = \sqrt{\frac{c_{44}(q_\perp)}{c_{66}(q_\perp)}}\,\frac{1}{q_\perp} \qquad (4)$$

Plots of $\cosh^{-1}[G_6(q_\perp)/G_6(q_\perp, L)]$ calculated from the two-sided decoration data at 5 and 12 G (Fig. 3) increase linearly with $q_\perp$ and then roll over as $q_\perp$ approaches the first reciprocal lattice vector. Using the linear slope of these plots and the values of c_{44} determined from our analyses of the density correlations, we find that values of c_{66} at 5 and 12 G are 1.4×10^{-3} and 5.0×10^{-3} G^2, respectively.

The experimental values of the elastic moduli determined at 5, 12, and 24 G are summarized in Table 1. These data show that the magnitude of c_{44} is much greater than c_{11} and c_{66} in this low–magnetic field regime. This difference between the absolute magnitudes of c_{44} versus c_{11} and c_{66} is notable because conventional models of rigid flux

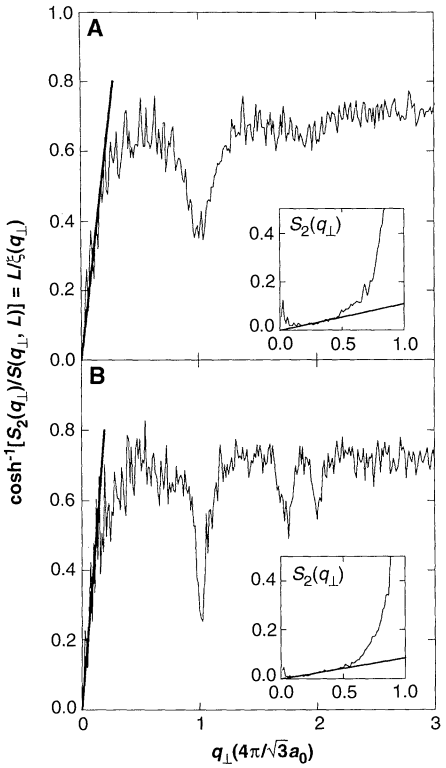

Fig. 2. Plots of $\cosh^{-1}[S_2(q_\perp)/S(q_\perp, L)] = L/\xi_\parallel(q_\perp)$ versus $q_\perp$ from the analysis of two-sided decoration data obtained in magnetic fields of (**A**) 5 G and (**B**) 12 G. The solid black lines are linear fits of the long-wavelength regime of these data; the slope of these lines equals $L\sqrt{c_{11}/c_{44}}$. The insets show the corresponding plots of $S_2(q_\perp)$ for $q_\perp$ less than the first reciprocal lattice vector. The black lines correspond to linear fits of the long-wavelength regime of the data; the slope of these lines equals $n_0k_BT/2\sqrt{c_{11}c_{44}}$. $S(q_\perp, L) = \langle\rho(q_\perp, L)\rho^*(q_\perp, 0)\rangle$ and $S_2(q_\perp) = \langle\rho(q_\perp, 0)\rho^*(q_\perp, 0)\rangle$, where $\rho(q_\perp, z)$ is the Fourier transform of the flux-line positions in a constant z cross section. The abscissa in all of these plots are in units of the reciprocal lattice vector, $4\pi/\sqrt{3}\,a_0$, where a_0 is the average spacing between vortices.

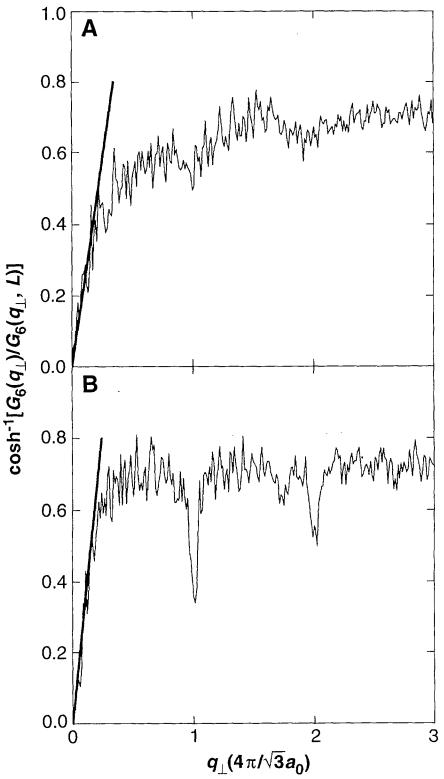

Fig. 3. Plots of $\cosh^{-1}[G_6(q_\perp)/G_6(q_\perp, L)]$ versus $q_\perp$ from the analysis of two-sided decoration data obtained in applied magnetic fields of (**A**) 5 G and (**B**) 12 G. The factor $G_6(q_\perp)$ is the 2D orientational correlation function calculated from a single (side) image, and $G_6(q_\perp, L)$ is the 3D correlation function calculated from both sample sides. The solid black lines are linear fits of the long-wavelength regime of this data; the slope of these lines equals $L\sqrt{c_{66}/c_{44}}$. The abscissa in these plots are in units of the reciprocal lattice vector, $4\pi/\sqrt{3}\,a_0$.

Table 1. Elastic moduli of the flux-line lattice in BSCCO as a function of magnetic field.

Magnetic field (G)	Elastic moduli (G^2)		
	c_{11}	c_{44}	c_{66}
5	1.8×10^{-3}	1.0	1.4×10^{-3}
12	8.0×10^{-3}	4.8	5.0×10^{-3}
24	2.8×10^{-2}	8.1	9.6×10^{-3}

lines or 2D pancake vortices, which have been used extensively to treat flux lines in the high transition temperature materials, predict that they should be of comparable magnitude (*2–5*). The similarities and differences of these experimental data have been compared (Fig. 4) with theoretical values calculated with Ginzburg-Landau (G-L) theory (*4*). The elastic moduli obtained from our experiments follow the same field dependence given by the G-L theory (that is, $c_{11} \propto B^2$, $c_{44} \propto B$, and $c_{66} \propto B$), indicating that underlying physical interactions are similar. However, this analysis shows that the magnitudes of the experimental c_{11} and c_{66} are about three orders of magnitude smaller than those predicted by G-L theory, although c_{44} agrees well with theory.

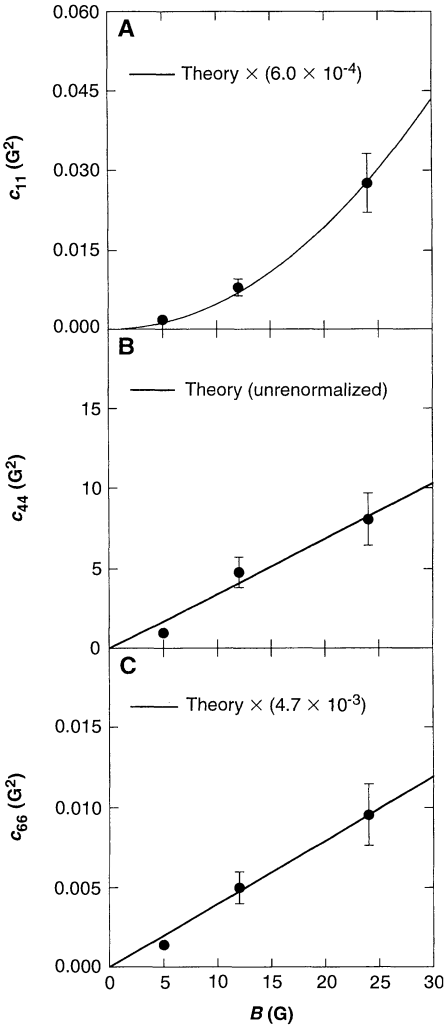

Fig. 4. Experimental values (circles) and theoretical predictions (lines) of the (**A**) compressional (c_{11}), (**B**) tilt (c_{44}), and (**C**) shear (c_{66}) moduli versus magnetic field B. The theoretical curves for c_{11} ($-B^2/4\pi$) and c_{66} ($-\phi_0 B/64\pi^2\lambda^2$) were multiplied by factors of 6.0×10^{-4} and 4.7×10^{-3}, respectively, to fit the experimental data. The theoretical fit $\phi_0 B/16\pi^2\lambda^2$ to the experimental data for c_{44} is not renormalized. The theoretical fits correspond to the long-wavelength limit of the analytical expressions for the wave vector–dependent elastic moduli (34). The value of $\lambda(T)$ used to calculate c_{44} and c_{66} is 0.62 μm and corresponds to a temperature of $0.97T_c$ (T_c, transition temperature).

The above results indicate that both c_{11} and c_{66} undergo a large downward renormalization in BSCCO. We believe that the origin of this renormalization may be thermal fluctuations. In particular, the renormalization of c_{11} can be qualitatively attributed to an entropic factor where the increased number of configurations arising from flux-line wandering and entanglement partially offsets the B^2 energy term. A theoretical analysis of the entropic and energetic contributions to c_{11} (*12*) and previous studies of flux-line interstitials (*17*) show explicitly the importance of the entropic factor, although more work is clearly needed to understand quantitatively this fascinating observation. Thermal fluctuations have also been studied previously to investigate flux-line melting (*2–5*), although fluctuation effects on the elastic moduli were not considered in this work (that is, the values from G-L theory were used). Hence, the large renormalization of c_{11} and c_{66} that we observe should lead to important corrections to the low-field region of the calculated flux-line lattice melting line. More generally, we believe that the two-sided decoration and analysis techniques reported herein will also have applications to studies of other copper oxide materials such as $YBa_2Cu_3O_7$, conventional superconductors, and flux-line pinning.

Lastly, the $q_\perp$-dependent spectrum of flux-line correlations is similar to the extensively studied phonon-roton excitation spectrum of superfluid ^{4}He. In superfluid ^{4}He, the wave vector–dependent excitation energy $\epsilon(q)$ increases linearly for small q, rolls over and exhibits a dip at a value of q corresponding to the average interatomic separation, and then increases again at larger q (*18*). The initial linear increase in $\epsilon(q)$ corresponds to phonon excitations, and the dip has been attributed to a "roton" excitation, whose microscopic origin remains controversial. These features are remarkably similar to those exhibited by our data for the disordered flux-line state in Fig. 2A. This similarity seems surprising because the flux lines are classical wiggling lines, whereas superfluid ^{4}He is a quantum liquid. However, it has been reported that the imaginary time trajectories of a 2D boson liquid (for example, ^{4}He) can be mapped onto the z-dependent positions of flux lines in a superconductor (*19*). By this mapping, the correlation length $\xi_\parallel(q_\perp)$ describing the decay of in-plane translation order is related to the flux-line excitation energy $\epsilon(q)$ as

$$\frac{1}{\xi_\parallel(q_\perp)} = \frac{\epsilon(q_\perp)}{k_B T} \qquad (5)$$

Hence, our Fig. 2A corresponds to a plot of $\epsilon(q_\perp)$ versus $q_\perp$ like the q-dependent excitation spectrum of superfluid ^{4}He. In the flux-line system, the linear "phonon" part of the spectrum corresponds to long-wavelength decay of density correlations along the sample z coordinate, while the roton dip corresponds to an enhanced propagation of flux-line correlation at the reciprocal lattice vector. Hence, the nature of the roton minimum, which has been controversial in superfluid ^{4}He, is in fact well defined in the flux-line system. Although more theoretical and experimental work are needed to understand the flux line–superfluid analogy, we believe that these results suggest a richness that may extend beyond the problem of flux lines.

REFERENCES AND NOTES

1. D. J. Bishop, P. L. Gammel, D. A. Huse, C. A. Murray, *Science* **255**, 165 (1992).
2. D. S. Fisher, M. P. A. Fisher, D. A. Huse, *Phys. Rev. B* **43**, 130 (1991).
3. G. Blatter, M. V. Feigel'man, V. B. Geshkenbein, A. I. Larkin, V. M. Vinokur, *Rev. Mod. Phys.* **66**, 1125 (1994).
4. D. S. Fisher, in *Phenomenology and Applications of High-Temperature Superconductors*, K. S. Bedell, M. Inui, D. Meltzer, J. R. Schrieffer, S. Doniach, Eds. (Addison-Wesley, New York, 1992), p. 287.
5. E. H. Brandt, *J. Supercond.* **6**, 201 (1993); *Phys. Rev. Lett.* **63**, 1106 (1989).
6. D. R. Nelson, in (*4*), p. 187.
7. Z. Yao, S. Yoon, H. Dai, S. Fan, C. M. Lieber, *Nature* **371**, 777 (1994).
8. D. R. Nelson and P. Le Doussal, *Phys. Rev. B* **42**, 10113 (1990).
9. C. A. Bolle *et al.*, *Phys. Rev. Lett.* **66**, 112 (1991).
10. I. V. Grigorieva, J. W. Steeds, K. Sasaki, *Phys. Rev. B* **48**, 16685 (1993).
11. H. Dai, S. Yoon, J. Liu, R. C. Budhani, C. M. Lieber, *Science* **265**, 1552 (1994).
12. M. C. Marchetti and D. R. Nelson, *Phys. Rev. B* **47**, 12214 (1993); *ibid*, in press.
13. The hydrodynamic model was derived originally for flux liquids. Because this model is also applicable to hexatic and crystalline flux-line arrays away from reciprocal lattice vectors, there is no loss in generality in its application to the present data (*8, 12*).
14. Several assumptions were made to arrive at Eqs. 2 and 3. Surface contributions to $R(q_\perp, L)$, which arise from the coulomb-like interactions between flux-line ends, have been ignored. Similarly, it is assumed that $S_2(q_\perp)$ corresponds to a 2D slice of the bulk flux-line array. For the range of $q_\perp$ evaluated in our experiments, these assumptions are believed to be reasonable (*12*). In addition, the contribution of flux pinning by point crystal defects was ignored because the flux-line array is frozen at a temperature close to the irreversibility line, where point pinning is believed to be weak (*8*).
15. The temperature relevant to the analysis of these experiments was determined from the $\cosh^{-1}[S_2(q_\perp)/S(q_\perp, L)]$ versus $q_\perp$ data. The point at which these plots deviate from linearity corresponds to $q_\perp \approx \lambda^{-1}(T)$; that is, the wave vector at which the repulsive interactions between flux lines or nonlocality in $c_{11}(q_\perp)$ becomes important. We estimate that $\lambda(T) \approx 0.6$ μm by this criteria. The temperature obtained by extrapolating from $\lambda(0)$ to $\lambda(T)$ with the two-fluid model is $0.97T_c$ or 80 K.
16. The bond orientational correlation functions that probe orientational order across the sample and on a single side are given by $G_6(q_\perp, L) = \langle \Psi_6(q_\perp, L)\Psi_6^*(q_\perp, 0)\rangle$ and $G_6(q_\perp) = \langle \Psi_6(q_\perp, 0)\Psi_6^*(q_\perp, 0)\rangle$, respectively. The factor $\Psi_6(q_\perp, L)$ is the Fourier transform of the bond orientational order parameter $\Psi_6(\mathbf{r}) \equiv \exp[6i\theta(\mathbf{r})]$ defined at the midpoint of a "bond" connecting two

nearest flux lines in a constant z cross section (6). Both $G_6(q_\perp)$ and $G_6(q_\perp, L)$ have peaks (delta function) at $q_\perp = 0$. These peaks are effectively removed when taking the ratio of these two quantities to obtain the transfer function $R_H(q_\perp, L)$; however, we have been unable to determine reliably the small-q behavior of $G_6(q_\perp)$ alone (that is, to extract $\sqrt{c_{44}c_{66}}$ as was done in the case of 2D density correlations for $\sqrt{c_{11}c_{44}}$ because of this peak.

17. E. Frey, D. R. Nelson, D. S. Fisher, *Phys. Rev. B* **49**, 9723 (1994).
18. R. K. Pathria, *Statistical Mechanics* (Pergamon, New York, 1993).
19. D. R. Nelson, *Phys. Rev. Lett.* **60**, 1973 (1988); M. P. A. Fisher and D. H. Lee, *Phys. Rev. B* **39**, 2756 (1989).

20. We thank D. R. Nelson and M. C. Marchetti for helpful discussions. C.M.L. acknowledges support by the National Science Foundation (grant DMR 9306684) and the Materials Research Science and Engineering Center Program of the National Science Foundation (grant DMR 9400396).

10 May 1995; accepted 18 August 1995

A Class of Cobalt Oxide Magnetoresistance Materials Discovered with Combinatorial Synthesis

Gabriel Briceño, Hauyee Chang, Xiaodong Sun, Peter G. Schultz,* X.-D. Xiang*

The recent development of methods for generating libraries of solid-state compounds has made it possible to apply combinatorial approaches to the discovery of materials. A library of 128 members containing different compositions and stoichiometries of $Ln_xM_yCoO_\delta$, where Ln = Y or La and M = Pb, Ca, Sr, or Ba, was synthesized by a combination of thin-film deposition and physical masking techniques. Large magnetoresistance has been found in $La_x(Ba,Sr,Ca)_y$-CoO_δ samples, whereas Y-based samples exhibit much smaller magnetoresistive effects. The magnetoresistance of the Co-containing compounds increases as the size of the alkaline earth ion increases, in sharp contrast to Mn-containing compounds, in which the magnetoresistance effect increases as the size of the alkaline earth ion decreases.

The discovery of the magnetoresistive effect (*1*) in Mn-based perovskite oxides $(La,R)_{1-x}A_xMnO_{3-\delta}$, where R is a rare earth element and A = Ca, Sr, or Ba, has attracted considerable attention because of the potential application of these materials in magnetic storage technology. Colossal magnetoresistance (CMR), with MR ratios $\Delta R/R(0) = [R(H = 0) - R(H)]/R(H = 0)$ as large as 99.0, 99.9, and 99.99%, have been reported for polycrystalline samples of $La_{0.60}Y_{0.07}Ca_{0.33}MnO_x$ and epitaxial thin films of $La_{0.67}Ca_{0.33}MnO_3$ and $Nd_{0.7}Sr_{0.3}MnO_{3-\delta}$, respectively (*2–4*). A large number of theoretical and experimental efforts have been undertaken to understand this unexpected phenomenon and to improve the room-temperature sensitivity, $[\Delta R/R(0)]/\Delta H$, at $H = 0$ of these materials, an important factor for technical applications. The question arises whether these effects are unique to Mn-based perovskite oxides or can be found as an intrinsic property of other materials.

We have applied a combinatorial approach (*5*) to the search for more CMR materials. Our initial search for CMR compounds was around simple perovskite ABO_3 and related A_2BO_4 or $A_{n+1}B_nO_{3n+1}$ higher order structures, where A = (La, Y, or rare earth)$^{+3}$ partially substituted with (Ca, Sr, Ba, Pb, or Cd)$^{+2}$ and B = (Mn, V, Co, Ni, Cr, or Fe). In this report, we describe a specific example of the generation and screening of one such library that resulted in the discovery of a family of Co-containing CMR materials. An analysis of the effects of spin configuration and electronic structure on the MR properties of the Co- and Mn-based compounds should help to elucidate the underlying mechanism of the CMR effect. Moreover, the discovery of diverse classes of the CMR materials may help efforts to optimize these materials for eventual device applications.

A 128-member library was generated by combining sequential radio-frequency sputtering deposition of thin films with a series of physical masking steps designed to produce Y-, La-, Ba-, Sr-, Ca-, and Co-containing films (1 mm by 2 mm) with varying compositions and stoichiometries (Fig. 1). Polished (100) $LaAlO_3$ single crystals were used as substrates and La_2O_3, Y_2O_3, $BaCO_3$, $SrCO_3$, CaO, and Co were used as sputtering targets (*6*). Two identical libraries (L1 and L2) were generated simultaneously and then thermally treated under different annealing and sintering

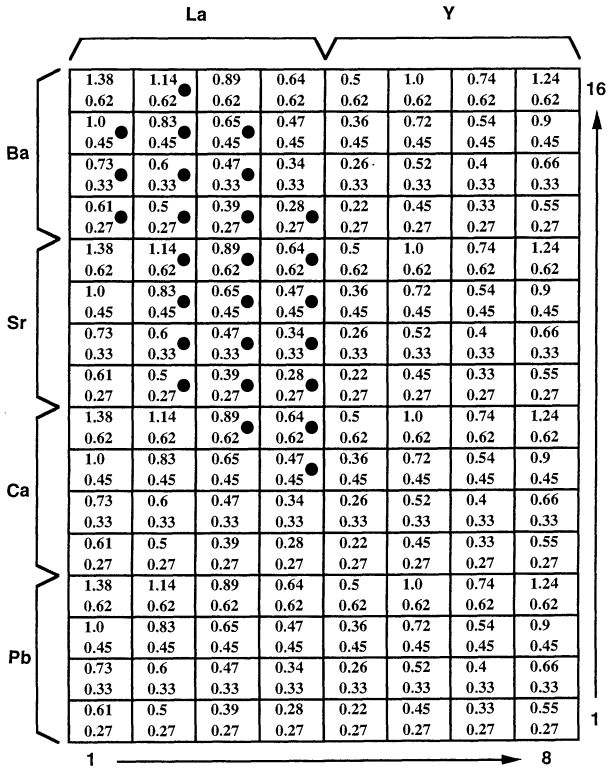

Fig. 1. A map of compositions and stoichiometries (Ln_xM_y-$CoO_{3-\delta}$, where Ln = La or Y and M = Ba, Sr, Ca, or Pb) of thin-film samples in libraries L1 and L2. Samples are labeled by index (row number, column number) in the text and figure legend. The first number in each box indicates x and the second y. Solid circles indicate the samples that show significant MR effects (>5%).

G. Briceño and X.-D. Xiang, Molecular Design Institute, Lawrence Berkeley Laboratory, Berkeley, CA 94720, USA.
H. Chang, X. Sun, P. G. Schultz, Molecular Design Institute, Lawrence Berkeley Laboratory, Howard Hughes Medical Institute, and Department of Chemistry, University of California, Berkeley, CA 94720, USA.
*To whom correspondence should be addressed.